



Spatial structure and wavenumber filtering of wall pressure fluctuations on a full-scale cockpit model

Simon L. Prigent¹ · Édouard Salze¹ · Emmanuel Jondeau¹ · Christophe Bailly¹

Received: 31 March 2020 / Revised: 19 June 2020 / Accepted: 16 July 2020
© Springer-Verlag GmbH Germany, part of Springer Nature 2020

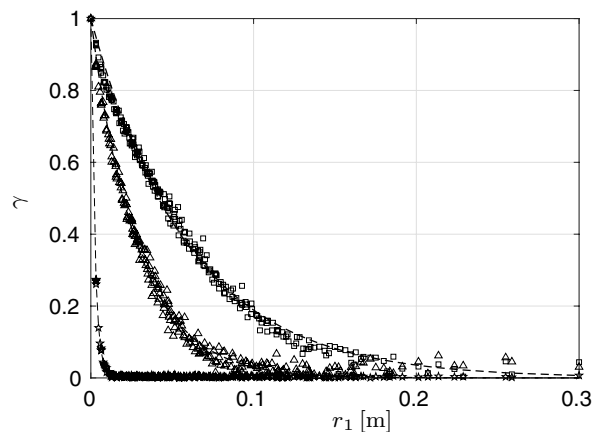
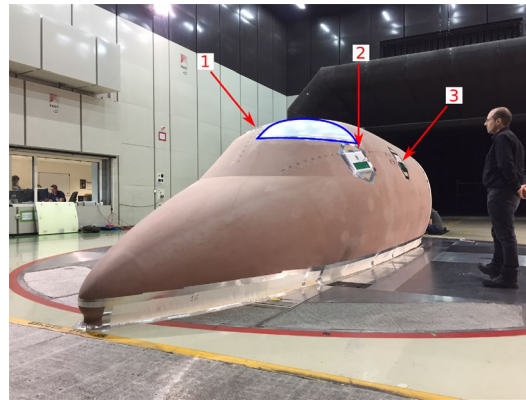
Abstract

Measurements of wall pressure fluctuations have been performed with arrays of MEMS microphones on a full-scale model of a business jet fore part. The boundary layers are characterised in terms of mean and root-mean-square velocity profiles and key parameters are computed to serve for the normalisation of pressure-related quantities. Frequency spectra are compared with classical models and strong discrepancies are highlighted, which are attributed to the non-canonical state of the boundary layers. The spatial structure of the pressure field is first characterised by the study of coherence and associated length scales. The hypothesis of auto-similarity on only one parameter, that is the frequency normalised by the separation to convective velocity ratio, is proven to reach its limits in the present case. In turn, the coherence length scales do not exhibit the classical -1 power law decay with frequency. The wavenumber–frequency formalism is used to differentiate the acoustic and hydrodynamic components of the pressure fluctuations in the spectral space. In the presence of an external acoustic source, the acoustic components are correctly extracted from the total field by spectral filtering, and the resulting frequency spectra are satisfactorily checked against the purely acoustic reference spectrum.

✉ Simon L. Prigent
simon.prigent@ec-lyon.fr

¹ Laboratoire de Mécanique des Fluides et d'Acoustique,
UMR 5509, Ecole Centrale de Lyon, 36 avenue Guy de
Collongue, 69130 Ecully, France

Graphic abstract



1 Introduction

Wall pressure fluctuations beneath a turbulent boundary layer are involved in many phenomena related to their diverse nature: hydrodynamic or acoustic; and in turn to their effect on the impacted surface. In the case of vehicles moving through air, their surface is loaded by these fluctuations. This creates a vibro-acoustic problem in which the excitation generates noise radiation, such as cabin noise in a cruising aeroplane, or structural damages in some more extreme cases. Underwater, these fluctuations can also pollute the signal received by a sonar system.

This topic has therefore attracted the attention of researchers during several decades (Bull 1996; Willmarth 1975). While some questions remain unanswered, such as the spectral level in the sub-convective area or the scaling of pressure fluctuations' root-mean-square values with Reynolds number; first understandings have been reached for the simple case of a flat plate with zero-pressure gradient. Models have been proposed for both the frequency content (Goody 2004) and spatial structure (Corcos 1963) of these fluctuations.

One of the major challenge is the understanding of pressure gradient effect. Measurements have been conducted (Salze et al. 2014; Schloemer 1967) and semi-empirical models proposed (Catlett et al. 2016; Hu 2018; Lee 2018; Rozenberg et al. 2012) but the topic is still debated. For instance, a recent numerical study (Cohen and Gloerfelt 2018) has offered a better understanding of the topic for flat plates with pressure gradients. The authors find no variation of the broadband convective velocity with pressure gradient, which appears to contradict previous findings (Schloemer 1967). Performing numerical simulations that capture the full range of pressure fluctuations is a strenuous task, and thus only a few are available.

Naturally, industrial applications often involve complex geometries that generate free stream pressure gradients. On top of this local parameter, the development of the boundary layer and sometimes its non-equilibrium state add to the difficulty of predicting or modelling the pressure fields. Measurements are therefore needed to gain an insight into the topology of pressure fields under such boundary layers. Maxit (2016) showed the importance of the sub-convective

content in vibro-acoustics. Bhat (1971) also highlighted that acoustic components of the wall pressure fluctuations played a role in cabin noise production. Therefore, the frequency content by itself appears to be insufficient, and the wavenumber–frequency formalism should be used since it enables the differentiated representation of acoustic and hydrodynamic components (Arguillat et al. 2010; Prigent et al. 2019; Salze et al. 2014).

Haxter and Spehr conducted in-flight measurements with arrays of Kulite pressure sensors placed on aluminium dummy side windows of the DLR test aircraft (Haxter and Spehr 2012, 2018). Despite the inherent challenges, they managed to measure the coherence and its spatial evolution, although low-separation values were not evolving smoothly. The resolution of the co-array in the direction of interest, limited by the sensors themselves and their arrangement, could have been a source of such oscillations. Two-dimensional wavenumber–frequency spectra were nonetheless computed and the authors later attempted to filter the acoustic components out of the total field.

The present study makes use of two main advantages of the newly developed MEMS microphones antenna: the sensors' small size enables a better resolution of the measurements, and the thin antenna can be placed onto the fuselage, without the constraint of placing them on dummy windows. By measuring the wall pressure fluctuations on the full-size mock-up of a real aeroplane, the aims of the present papers are twofold. First, from a technological point of view, the aim is to assess the use of such antennas in characterising the wall pressure fluctuations, to determine which quantities can be reliably measured. For instance, the ability to extract the acoustic components from the pressure fields by means of wavenumber filtering is tested. Second, the measured data is confronted to widely used models, both in terms of frequency spectra and coherence decay, to assess their validity for such non-canonical boundary layers. Conducting the measurements in a wind tunnel insures repeatability of the inflow conditions, and offers the possibility to work at relatively low speeds for which the pressure fluctuations are within the range of the currently existing MEMS microphones.

2 Apparatus

2.1 Mock-up and general layout

Measurements have been conducted in the S2A aeroacoustic wind tunnel near Paris, France. The closed-loop tunnel opens to a test room with an inlet section of 24 m². The test room itself is 15 m long and its walls are treated against acoustic reverberation. An outlet (seen in black in Fig. 1) then guides the air back into the loop. Results presented in

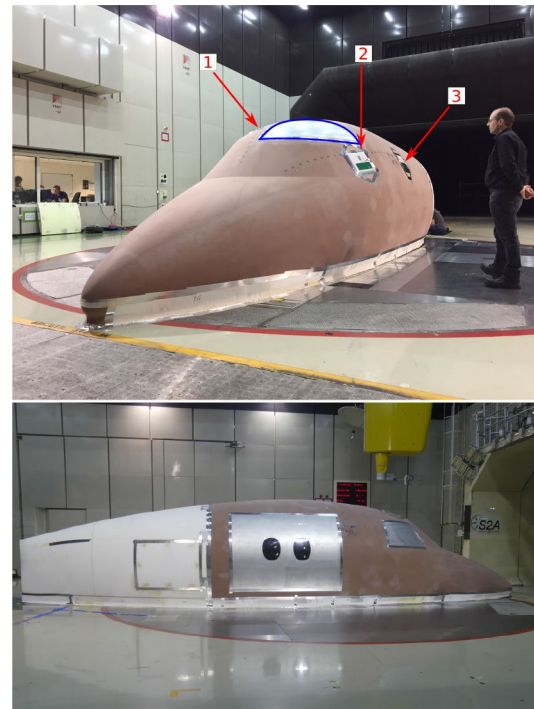


Fig. 1 Mock-up installed in the S2A wind tunnel with the location of the three modules

this paper have been measured with inlet velocities ranging from 15 to 65 m s⁻¹.

The mock-up used in this study is a full-scale fore part of a Dassault Aviation Falcon 2000 business jet. The mock-up is 10 m long in total, with the first 6 m true to the aeroplane geometry, and the remainder serving as a tail to streamline the rear end. The outer surface was milled to the geometry while static pressure sensors were fitted along some specific streamlines and two kinds of inserts were added. First, panels mimicking the vibrational behaviour of a real jet fuselage were added to the structure, and were equipped with accelerometers to study interior noise radiation. This latter topic is beyond the scope of the present paper. Second, modules supporting wall pressure microphone antennas, hot films, hot wires, a 1/8 in reference microphone and thermocouples were placed in locations mirroring those of the panels. Those three modules correspond, respectively, to the roof (1), windscreen (2) and side panel (3). Figure 1 shows these locations and the corresponding module numbers. Finally, the inside of the mock-up was hollowed to store electronics and allow for interior noise measurements.

2.2 MEMS antenna

Wall pressure measurements are made with antennas of MEMS microphones. Those are integrated in the modules supporting different sensors, as previously mentioned.

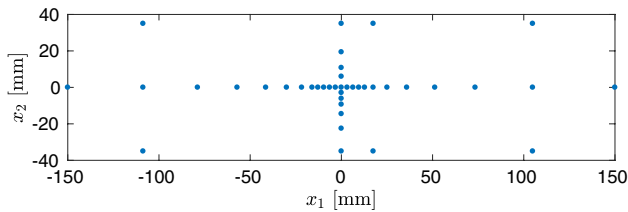


Fig. 2 Coordinates of the microphones on the electronic board

Naturally, the hot-wire traverse was removed during the acquisition of wall pressure data. The flat, 0.8-mm-thick, electronic board on which the microphones are affixed is flush-mounted onto a flare that is fitted to the outer geometry of the fuselage. The total added thickness is of 2.5 mm. Tests have been carried out in the anechoic wind tunnel at Ecole Centrale de Lyon, both with and without flare to assess the effect of the added thickness and the robustness of the technology at the targeted velocities (Salze et al. 2019).

Each antenna is composed of 40 digital microphones, most of which are non-uniformly distributed on a $70 \times 300 \text{ mm}^2$ cross whose main axis is aligned with the flow direction, and six are placed in the quadrants as depicted in Fig. 2. The microphones themselves are InvenSense's $4 \times 3 \times 1 \text{ mm}^3$ INMP621 digital microphones which output digital data. These bottom-port microphones are fitted to pinholes of diameter 0.6 mm. Further details on the digital architecture (clock generation and digital bus decoding) of such an array can also be found in the study by Salze et al. (2019). During each measurement run, data is sampled at 50 kHz for 120 s.

2.3 Hot-wire anemometry and hot film measurements

Velocity profiles of the boundary layers have been measured via hot-wire anemometry. The probe itself is a Dantec-55P01 whose 3-mm-long gold-plated wire includes a 1.25-mm active sensor of $5 \mu\text{m}$ diameter. Its support is mounted on a traverse system, normal to the mock-up surface that enables the automation of wall-normal displacement. Calibration has been performed prior to the probes' installation, in a portable calibration wind channel at temperatures close to that of the main wind tunnel. Minor discrepancies between operating and calibration temperatures are accounted for and their effect corrected in post-processing.

In addition, each module is fitted with six Senflex hot-films (ref. 93032) whose dimensions are $1.45 \times 0.10 \times 0.0002 \text{ mm}^3$. The skin friction can thus be directly measured and checked against the value obtained by fitting the velocity profiles. The hot films have been calibrated in a bespoke low aspect ratio channel flow: $1.6 \times 0.319 \times 0.015 \text{ m}^3$. For each calibration velocity, the

static pressure gradient is measured and thus the wall shear stress is computed.

This set-up is depicted in Fig. 3 where the whole measurement unit is visible.

3 Initial assessments and data reliability

3.1 Boundary layer measurements

The boundary layer was characterised for each target velocity. Friction velocities (u_τ) were obtained from fitted profiles and satisfactorily checked against those directly measured with hot films, see Table 1. The latter are computed by averaging data from all films on a given module and all runs at a given velocity. In addition, 64 static pressure (P) probes were placed along streamlines crossing the measurement locations, to directly measure the local pressure gradient. The non-dimensional Clauser pressure gradient parameter $\beta = (\delta_1/\tau_w)\nabla P$ indicates that the boundary layer over module 1 (roof) is subjected to an almost-zero pressure gradient, the one over module 2 (windscreen) to a mild favourable pressure gradient, and the one over module 3 (side panel) to a mild adverse one. The boundary layer thickness δ_{99} is taken as the distance from the wall at which the mean velocity is equal to $0.99 \times U_e$, where U_e is the local outer velocity. Displacement thickness (δ_1), momentum thickness (δ_2) and aspect ratio ($H_{1,2} = \delta_1/\delta_2$) are also reported.

The mean velocity profiles, expressed in wall units, $U^+ = \bar{U}/u_\tau$, obtained for the three modules, are shown in Fig. 4 for three inlet velocities (U_∞) 30, 45 and 65 m s^{-1} . They have been fitted using the method initially presented by Rodríguez-López et al. (2015), Esteban et al. (2017), with $\kappa = 0.41$. Profiles from the zero-pressure gradient (ZPG) Large Eddy Simulation (LES) FLOW group's database (Eitel-Amor et al. 2014) have been added for module

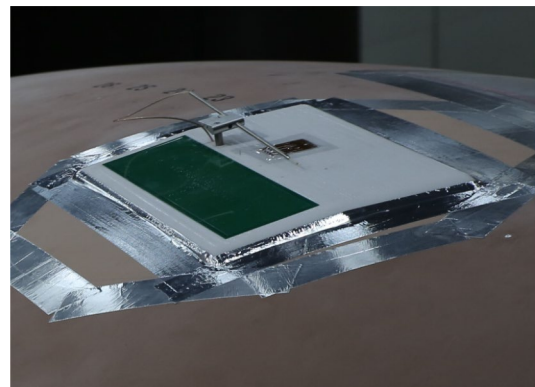


Fig. 3 Measurement module with the pressure antenna, the hot films, and fitted with a hot wire traverse

Table 1 Boundary layer parameters determined from hot-wire measurements

Module	1 (—)			2 (—)			3 (—)		
U_∞	30	45	65	30	45	65	30	45	65
δ_1	1.84	1.66	1.82	2.18	2.03	2.32	5.84	5.70	5.68
δ_2	1.36	1.24	1.32	1.62	1.51	1.98	4.34	4.21	4.15
$H_{1,2}$	1.35	1.34	1.38	1.34	1.34	1.38	1.35	1.36	1.37
δ_{99}	11.5	11.4	11.2	14.8	14.7	19.5	37.0	36.9	36.8
U_e	33.6	46.0	72.4	32.1	48.4	75.9	31.2	46.5	68.2
u_τ	1.30	1.76	2.61	1.24	1.79	2.67	1.09	1.55	2.14
u_τ^{hf}	1.22	1.79	2.42	1.27	1.87	2.64	1.20	1.92	2.64
$Re^+ \cdot 10^{-3}$	0.955	1.28	1.83	1.17	1.69	3.30	2.62	3.61	4.97
$Re_{\delta_1} \cdot 10^{-3}$	3.96	4.88	8.30	4.46	6.28	11.1	11.8	16.7	24.4
$\beta \cdot 10^2$	1.2	1.5	1.6	-6.8	-6.8	-7.2	6.4	5.9	4.8

Friction velocity obtained with hot films (u_τ^{hf}) is added for comparison; lengths in [mm] and velocities in [$m s^{-1}$]. Colour code provided for spectra and coherence length plots

1, which has the smallest values of β , at similar Reynolds number: $Re^+ = 957$ and $Re^+ = 1937$.

The boundary layers from modules 1 and 2 exhibit very similar profiles, reaching almost the same values and starting their plateau at the same normalised distance from the wall. It should be noted, however, that the velocity then tends to decrease. On the other hand, the profiles from module 3 exhibit a true plateau starting at higher values of y^+ . This is expected, as modules 1 and 2 are placed in similar positions in terms of distance from the nose, and both displacement thickness and friction velocity take similar values at both locations. Module 3 mirrors the side panel and is therefore further downstream, which explains its more developed state. This is clear in terms of Reynolds number, reported in Table 1 for both $Re^+ = u_\tau \times \delta_{99}/\nu$ and $Re_{\delta_1} = U_e \times \delta_1/\nu$, which are larger for module 3. When compared to ZPG LES data, profiles from module 1 deviate from the logarithmic law at smaller values of y^+ and reach higher wake values. Despite the weakness of the pressure gradient, these profiles do not exhibit the characteristics of a canonical boundary layer in the absence of free stream pressure gradient. Although the plateau in the outer region is stable for module 3, and the extent of its logarithmic region is larger, one notices that the mean velocity curves upwards in that region, which deviates from standard profiles. It should be noted that despite the relatively high values of Reynolds number found for all boundary layers, they have had to develop over the varying geometry of the fuselage. The impact this has had on their properties is not represented by local parameters such as the local pressure gradient, and although the shape factors are found at standard values, this aspect should be kept in mind as an explanation of their discrepancies with canonical boundary layers.

Figure 5 shows the velocity fluctuations' root-mean-square profiles, in wall units $u'_{rms} = u'_{rms}/u_\tau$, of the boundary

layers from the three modules at the three discussed inlet velocities. For module 1 (roof), LES data corresponding to the previous profiles is added for reference. The measured profiles are in good agreement with the LES data in the outer region, but the absence of near-wall peak is striking. All three modules exhibit similar profiles with a standard outer region, but a plateau in the logarithmic and near-wall regions. One could think that the absence of near-wall peak is due to the adverse pressure gradient since Harun (2012) reported a weakening of said peak with such gradient. However, these present gradients are weak and should not be a sufficient explanation on their own; especially for module 2 (windscreen) that has a mild favourable gradient. Hutchins et al. (2009) documented a filtering of the inner scales of turbulent fluctuations due to the finite size of the sensing wire l , written in wall units as $l^+ = l \times u_\tau/\nu$. This parameter takes rather high values for the present study, of 88 – 169 for module 3 (side panel) at the lowest and 104 – 205 for module 1 at the highest. Without pressure gradient, Hutchins et al. reported a significant reduction of the near-wall peak even at values of l^+ as low as 80. A different apparatus would have been needed to allow the study of turbulence intensity in the near-wall region, but this would have been beyond the scope of the present paper.

3.2 Wall pressure data

The measurements presented in this study were run at different times to accommodate for various configurations, for the study of interior noise. It is thus important to ensure good repeatability of the process. The spectra obtained for the same target velocity ($30 m s^{-1}$) but at different times, and even after moving the mock-up out of the wind tunnel and re-installing it, are presented in Fig. 6 for one microphone of module 3. All spectra are

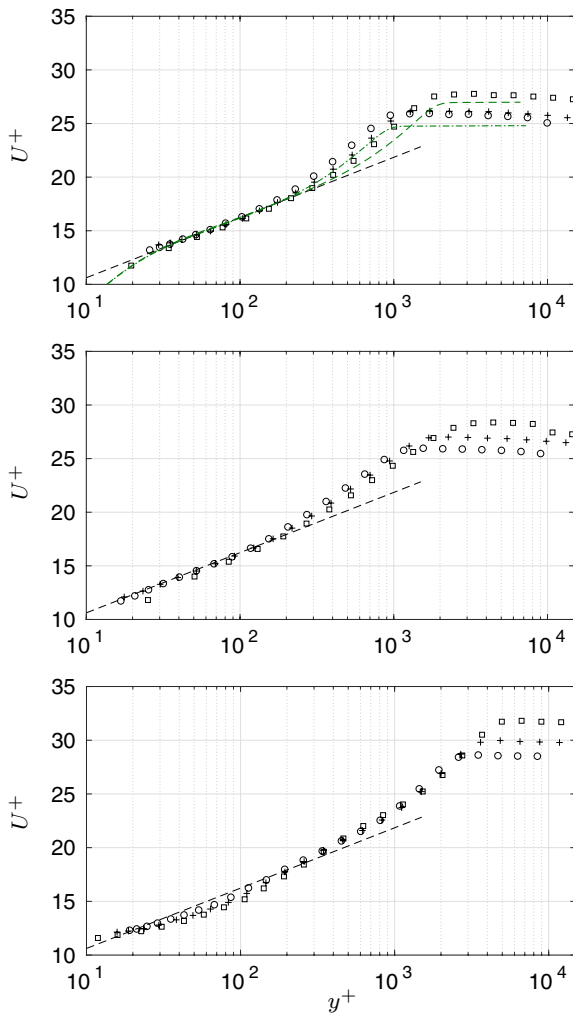


Fig. 4 Mean velocity profiles in wall units for the three modules, ordered from top to bottom, at (○) 30, (+) 45 and (□) 65 m s⁻¹. --- Log law with $\kappa = 0.41$ and $B = 5$. LES data from (KTH FLOW group 2019; Eitel-Amor et al. 2014) at (— · — ·) $Re^+ = 957$ and (— — —) $Re^+ = 1937$

corrected for pin-hole resonance and sensors’ size effects, see Appendices A & B. Signal is acquired for 120 s and spectra are computed using 958 rectangular windows of 250 ms with a 50 % overlap. It is clear that all measurements are close to identical, which speaks in favour of the reliability of the data. One notices that the acquisition time is long enough to render smooth spectra. Figure 6 also shows, for one dataset, the spectrum averaged over all microphones of the antenna and its standard deviation. The spectrum is found to be homogeneous over the antenna, which is a key property to enable further data processing such as wavenumber–frequency analysis, and to support some assumptions required for numerical simulations in vibro-acoustics. The spectra shown in the remainder of the article are averaged in the same way.

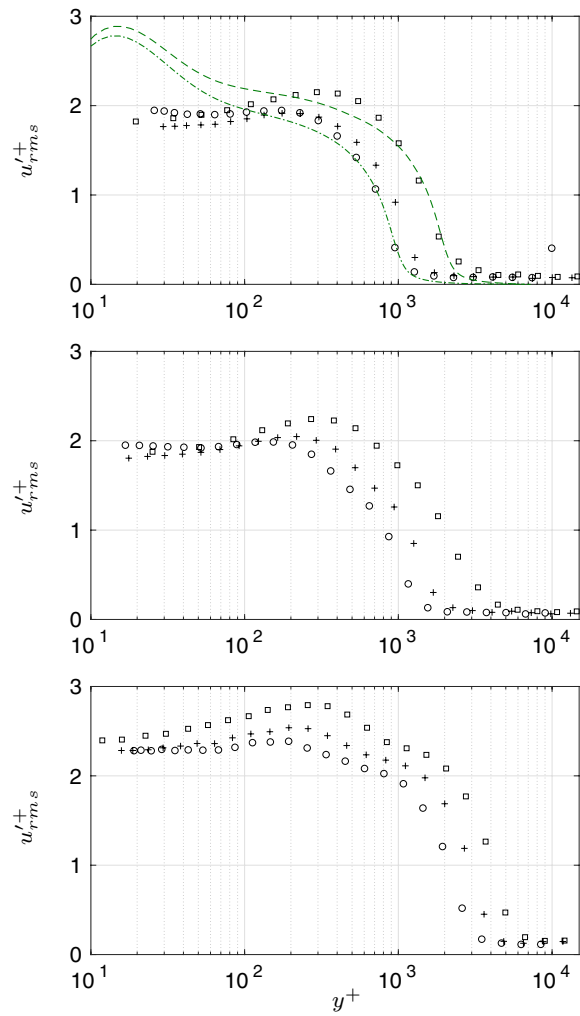


Fig. 5 Root-mean-square velocity profiles in wall units for the three modules, ordered from top to bottom, at (○) 30, (+) 45 and (□) 65 m s⁻¹. LES data from (KTH FLOW group 2019; Eitel-Amor et al. 2014) at (— — —) $Re^+ = 957$ and (— · — ·) $Re^+ = 1937$

The main limitation of the designed antenna is the sensors’ saturation which occurs for inlet velocities above 55 m s⁻¹, with a threshold of about 130 dB as expected from the manufacturer’s specifications.

4 Results

Little is known on the intensity of wall pressure fluctuations on a realistic fuselage; the auto-spectra thus appear as the first step to take towards their characterisation. Figure 7 shows the wall pressure spectra, averaged over all sensors of each modules, measured at 30 and 45 m s⁻¹, along with some corresponding values from the Goody (2004) and Lee (2018) models. The low-frequency limit for all spectra is set at 100 Hz, to avoid discussing a behaviour that could be

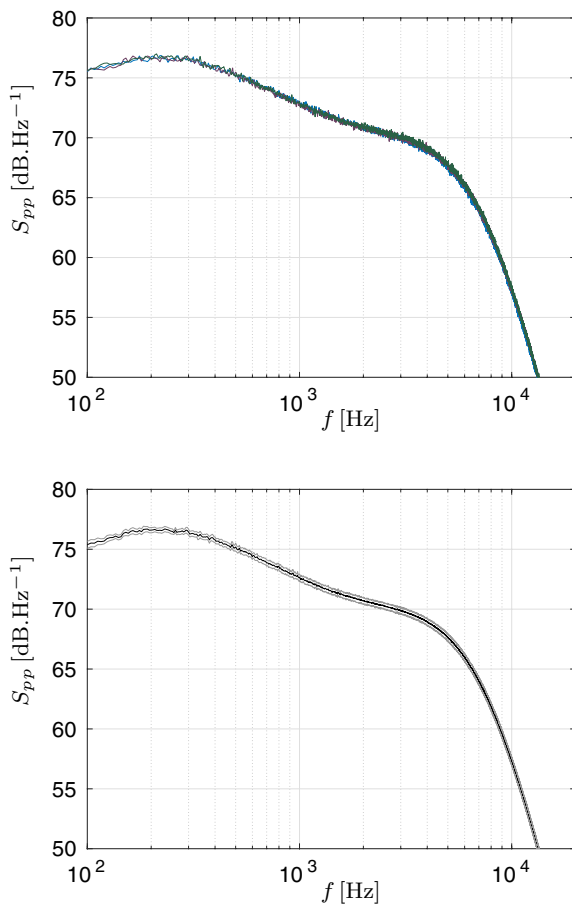


Fig. 6 Spectra of one microphone from three data sets (top) and spectra of all microphones from one data set: average and standard deviation (bottom), at 30 m s^{-1}

affected by the cut-off from the sensors, expected around 50 Hz. The present data has been corrected for its pinhole resonance using a second-order resonator, see Appendix B for more details.

Comparing the spectra at different locations, one notices that the ones from module 3 have an increased content at both ends of the mid-frequency range (about $3 \times 10^{-1} \leq \omega\delta_1/U_e \leq 6$ here) while the two others are flatter. As previously mentioned, the velocity profiles on module 1 and 2 are similar, so it is not surprising that the spectra should be similar too. The shape of the spectra, and in particular the slopes of the different regions that can be observed, is not that of a typical spectra from beneath a fully developed turbulent boundary layer. Spectra from modules 1 and 2 do not exhibit the typical -0.7 in the mid-frequency range, and are closer to a -0.2 decay. Their level also deviates from that predicted by both Goody (2004) and Lee models, the latter not being shown for readability.

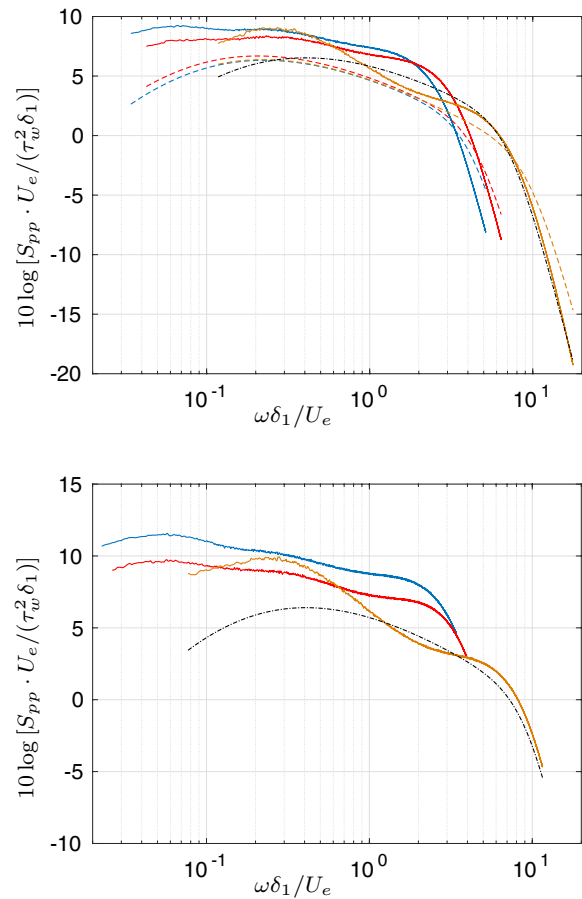


Fig. 7 Averaged, pinhole- and Corcos-corrected spectra at 30 m s^{-1} (top) and 45 m s^{-1} (bottom); for modules 1 (—) 2 (—) and 3 (—), and corresponding Goody model (dashed line). Lee model is added for module 3 (— · —)

Goody model was developed for a boundary layer on a flat plate without free stream pressure gradient, it is thus not surprising it should not fit the data. The discrepancy is of about 3–4 dB, and the original constants of the model have been used. On the other hand, the spectrum measured on module 3 is closer to levels predicted by Lee’s model. However, it strongly deviates from the model with the two bumps at the ends of the mid-frequency range. The spectra at 45 m s^{-1} are similar to the ones discussed for 30 m s^{-1} , and the same comments can be made, except that the discrepancies from predicted levels are increased, Goody model is not shown for readability.

4.1 Coherence

The intensity of the excitation alone does not provide a sufficient description, and its spatial structure is also of interest.

Under the assumption of homogeneity over the antenna, one can compute coherence with all available pairs of microphones and retain those resulting in unique separation vectors, instead of using a single reference microphone. Figure 8 shows the stream-wise coherence on module 3 at 30 m s⁻¹, at three frequencies, and an exponential decay fit. This exponential decay is the basis of the Corcos model, along with the separation of variables from both stream-wise and span-wise directions. Indeed, the Corcos model for the interspectra can be written as

$$S(\mathbf{r}, \omega) = S_{pp}(\omega)e^{-|r_1|/L_1}e^{-|r_2|/L_2}e^{ik_c r_1}, \tag{1}$$

where r_i and L_i represent the separation and coherence scale in the i th direction and the latter is bound by a similarity scaling assumption such that $L_1 = \alpha_1 U_c / \omega$. Fitting such a decay at each frequency therefore gives the stream-wise (or longitudinal) coherence scale. The frequency values that are displayed highlight the fact that at 400 Hz the extent of the antenna is large enough to enclose the tail of the coherence curve, while the minimum separations offer enough points to fit the exponential decay even at 5 kHz.

The coherence scales, both longitudinal and transverse, for all three modules at 30 m s⁻¹ and 45 m s⁻¹ are given in Fig. 9. First of all, the values for a given module does not seem to significantly vary with velocity when normalised by the displacement thickness. However, the coherence scale drastically changes from one module to the other. While the values for module 3 reach a low-frequency plateau which level of $L_1/\delta_1 \sim 20$ is similar to data measured on flat plates (Salze et al. 2014), module 1 in particular exhibits a strong decrease that differs from models' predictions.

The Corcos model's -1 power law is added and its level fitted to module 3's data. One notices the two main

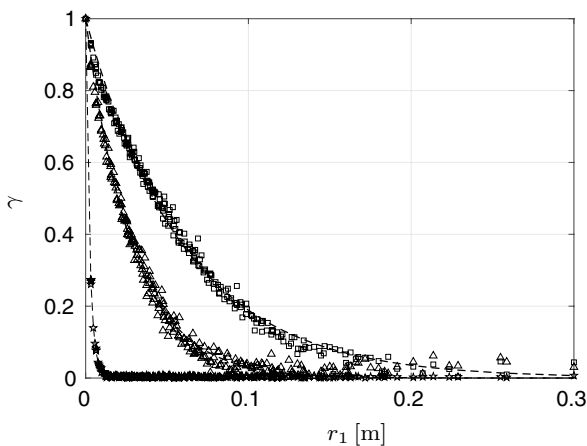


Fig. 8 Stream-wise coherence for module 3 at 30 m s⁻¹, at various frequencies: (□) 400 Hz; (Δ) 800 Hz; (★) 5 kHz, and corresponding exponential fit

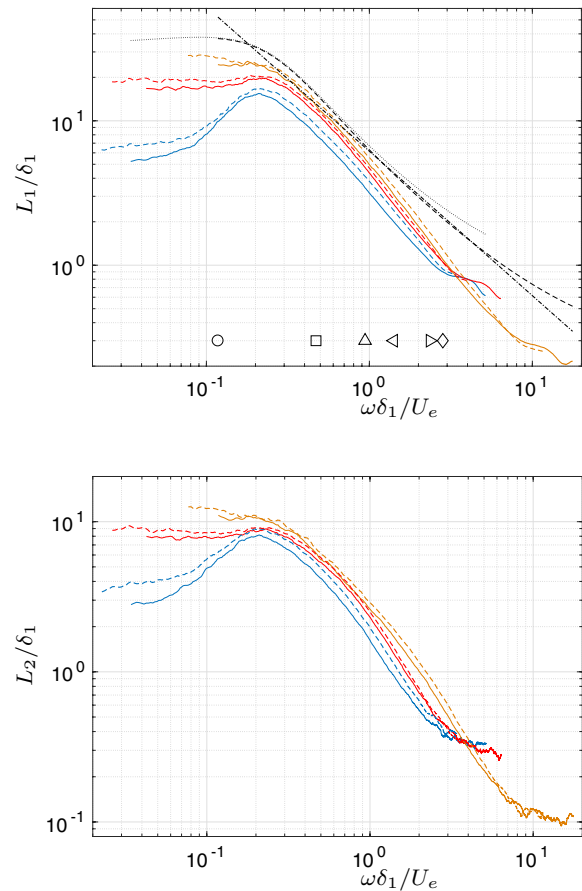


Fig. 9 Longitudinal (top) and transverse (bottom) coherence scales for modules 1 (blue), 2 (red) and 3 (yellow) at 30 m s⁻¹ (plain) and 45 m s⁻¹ (dashed). With Smol'yakov model based on ... module 1 and - - - module 3, and - . - Corcos model based on module 3. Symbols refer to frequencies displayed in Fig. 10 and partly in Fig. 8

limitations to this model. First, it does not account for the plateaux at both low and high frequencies. Second, the -1 power law does not correctly describe the decay rate of the present data outside the range $0.3 \leq \omega\delta_1/U_e \leq 0.8$. Out of fairness, it should be noted that this model was developed about 50 years ago to account for the spatial integration due to the size of the sensors. Should one use the Corcos model nonetheless, its parameters α_i can be adjusted to fit the level of the -1 power law decay curve: the corresponding values are reported in Table 2.

The Smol'yakov (2006) model is compared to the present data with parameters from both modules 1 and 3. The idea behind this model is to keep the basis of the Corcos model, and introduce limits of the scale at both low frequency, physically justified by the finiteness of the boundary layer thickness, and high frequency because of viscosity effect. While the measured data get closer to the model's prediction with increased Reynolds number (from

Table 2 Corcos coefficients fitted on coherence length scales

Module	1	2	3
U_∞	30	45	30
α_1	4.8	5.6	7.1
α_2	2.6	3.0	3.6

module 1 to 3), the discrepancy is not satisfactory. The original parameters of the model were used, but although they can be tuned to fit the experimental data in terms of convective velocity, the change in terms of coherence scale is minimal and the modified curves are not displayed to maintain the figure readability. Above $\omega\delta_1/U_\infty \geq 0.8$, the measured decay rates are consistently steeper than the expected -1 power law, contrarily to the model.

As pointed out, the Corcos model relies on the assumption that $L_1 = \alpha_1 U_c / \omega$ therefore should U_c be constant, it would exhibit a -1 power law. However U_c varies with frequency, as will be illustrated later on: the convective velocity can in fact be determined from the phase of the interspectra. For a given frequency, this phase almost linearly evolves with r_1 over an extent that varies with frequency. Its slope directly gives this velocity, as one can see in the study by Salze et al. (2014). This variation of convective velocity alone does not account for the observed deviation. Indeed, the measured frequency-dependent convective velocity has been inputted in both models, not shown here for readability. While it clearly changes the shape of the Corcos model, it does not recover the correct decay rate. The Smol'yakov model based on measured convective velocity is very close to the fully modelled one.

The discussed assumption is in fact based on a similarity scaling of the coherence, according to which it only depends on $\omega|r_i|/U_c$ such that

$$\gamma(r_1, \omega) = \exp\left(-\frac{\omega|r_1|}{\alpha_1 U_c}\right). \tag{2}$$

Figure 10 shows the coherence plotted against $\omega_0 r_1 / U_c$ for various frequencies. It shows a behaviour similar to what was presented by Farabee and Casarella (1991) where coherence tends to a similarity scaling after a frequency cut-off. They reported such a similarity for $\omega\delta_{99}/u_\tau \geq 50$ which, for the present data, corresponds to the displayed frequencies of at least 400 Hz. Indeed, the data for 100 Hz are clearly well below the exponential decay, while at 400 Hz a good collapse is observed. Farabee and Casarella (1991) also indicated that at high frequencies, the coherence tends to deviate from the similarity scaling. Such deviation is clearly visible in the present data, with a ratio of about 2 between the coherence at 400 and 2400 Hz for $\omega r_1 / U_c = 10$. This deviation from the similarity scaling questions the premise

of the discussed models and could therefore explain why the expected -1 power law is not found.

4.2 Wavenumber–frequency spectra

A means of characterising both spatial and temporal structures of the fluctuations is the computation of the wavenumber–frequency spectra. It is, by definition, the Fourier transform of the spatio-temporal correlation function, and is in practice evaluated by Fourier transforming the cross-spectra in space. The Fourier transformation along the non-uniformly distributed line of microphones is done using the same numerical method as described in Prigent et al. (2019) for a rotating antenna. A local incremental length is attributed to each separation in the co-array of the antenna. A Blackman–Harris window is applied to the separation vector to reduce oscillations of the transfer function of the array.

Figure 11 shows the one-dimensional wavenumber–frequency spectra for module 3, i.e. at the location mirroring that of the side panel. The convective wavenumber is obtained from the discussed convective velocity. For reference, a wavenumber based on the assumption of constant

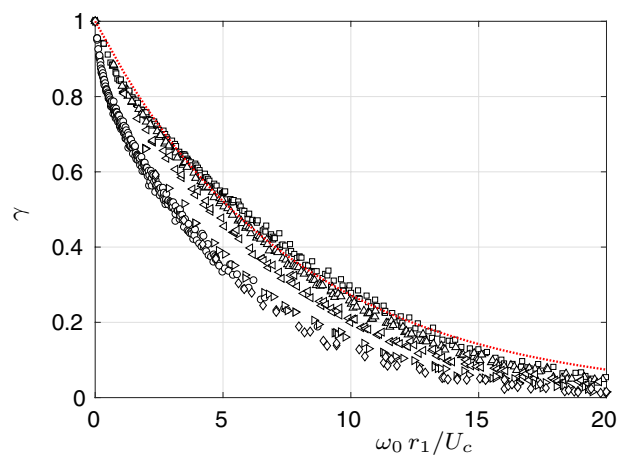


Fig. 10 Stream-wise coherence for module 3 at 30 m s^{-1} , at various fixed frequencies: (\circ) 100 Hz, $\omega\delta_{99}/u_\tau = 22.1$; (\square) 400 Hz, $\omega\delta_{99}/u_\tau = 85.1$; (\triangle) 800 Hz, $\omega\delta_{99}/u_\tau = 170$; (\triangleleft) 1200 Hz, $\omega\delta_{99}/u_\tau = 255$; (\triangleright) 2000 Hz, $\omega\delta_{99}/u_\tau = 426$; (\diamond) 2400 Hz, $\omega\delta_{99}/u_\tau = 511$. (\cdots) Exponential decay according to Eq.(2) with $\alpha_1 = 7.7$

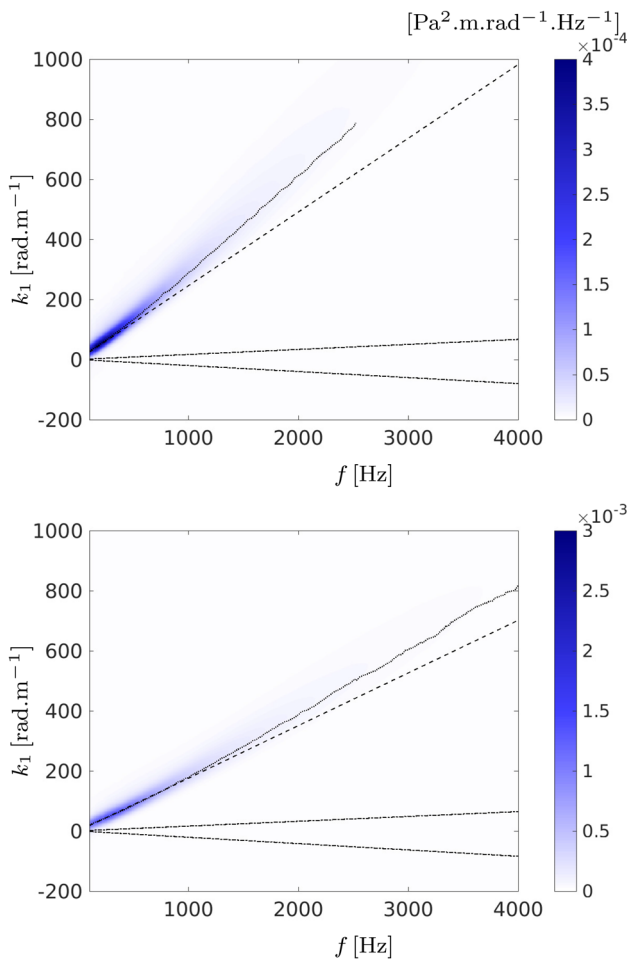


Fig. 11 Wavenumber–frequency spectra at 30 (top) and 45 m s⁻¹ (bottom), for module 3. (— —) $k_c = 2\pi f / (0.8 \times U_e)$ and (····) measured k_c added for reference. (— · · ·) acoustic ellipse

convection velocity is taken as $k_c = 2\pi f / (0.8 \times U_e)$ at 30 and 45 m s⁻¹. The bounds of the acoustic ellipse are added with dash-dotted lines, following:

$$k_{ell} = k_0 \times \frac{(-U_e/c_0 \pm 1)}{1 - (U_e/c_0)^2}, \tag{3}$$

with k_0 the acoustic wavenumber and c_0 the speed of sound.

It is clear that the real convective wavenumber does not depend linearly on frequency, thus illustrating the point made earlier on the variation of $U_c(\omega)$. The convective ridge is clearly visible on the $k_1 - f$ maps; however, no acoustic component can be found. The maps are overall clearly measured, which would be helpful should one use them as inputs for vibroacoustic applications. One should note that data has not been deconvolved but was windowed in space prior to Fourier transforming to limit oscillations that are due to the antenna’s transfer function, as detailed by Prigent et al.

(2019). Similar results, not shown here for brevity, had been obtained in a preliminary design phase of the technology, but in research facilities with a channel flow mounted in the anechoic wind tunnel of the Fluid Mechanics and Acoustics Laboratory (LMFA) at Ecole Centrale de Lyon.

The corresponding spectra for modules 1 and 2 are not shown here: they exhibit a similar structure as the ones from module 3, but have lower levels at the given velocities, and their associated convection velocity is lower. This is in fact logical since pressure spectra already exhibited lower levels, and the mean velocity profiles had shown lower values.

Combining all microphones from the antenna gives a two-dimensional map of the cross-spectra. However, given that this is not the intended use of the antenna, the resolution in separation (\mathbf{r} vector) is inhomogeneous, and coarse in some areas. Rather than the classical separation of variables in the exponential decay postulated by Corcos, this set of data appear closer to an elliptical exponential decay. This observation is not new, and the map is therefore not shown here for brevity. Such a formulation is the basis of the Mellen model Mellen (1990) which would therefore seem better suited to fit the cross-spectra. However, this does not question the use of the Corcos model in accounting for the sensors’ diameter: as shown in Appendix A, using one model or the other has close to no effect on the correction in the current conditions.

5 Impinging acoustic waves

Acoustic waves generated outside of the boundary layer can impinge on the wall and contribute to the pressure field. For instance, an aeroplane’s communication antennas protrude from its fuselage and are a source of noise. Naturally, the characterisation of such sources depends on the devices’ geometry and is therefore beyond the scope of the present article. However, to assess the ability of the microphones’ antenna to detect their effect on wall pressure, a more controlled test case has been used.

An acoustic source was placed in the wind tunnel, slightly upstream of the mock-up and on both sides consecutively. The one-dimensional wavenumber–frequency spectra are displayed in Fig. 12. When the source is placed on starboard side, the antenna is shielded by the mock-up and indeed no acoustics can be seen. On the other hand, when the source is placed on port side the spectrum is clearly modified. It is worth noticing that all the acoustic components from this spectrum are located in the positive wavenumber region, which means the corresponding waves are travelling downstream, which indeed corresponds to the set-up. Since the waves arrive on the module at an incidence and only their k_1 component is measured, the corresponding wavenumbers are lower than the acoustic wavenumber.

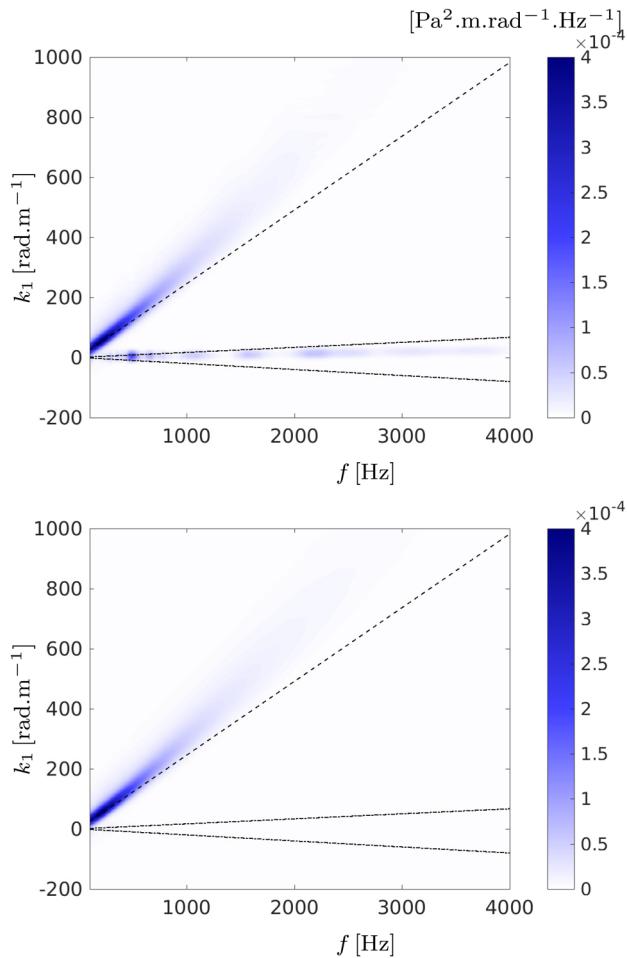


Fig. 12 Wavenumber–frequency spectra for module 3 at 30 m s⁻¹, with acoustic source on port (top) and starboard (bottom). (— — —) $k_c = 2\pi f / (0.8 \times U_c)$ and (— · — ·) acoustic ellipse

One of the main advantages of the wavenumber–frequency formalism is that it enables distinguishing hydrodynamic from acoustic components. The spectrum can then be filtered to only keep the component of interest. Figure 13 shows the auto-spectra obtained by integrating the acoustic components and filtering out the hydrodynamic ones, at two inlet velocities when the acoustic source is on. It also shows the spectra measured with the acoustic source, with and without flow. The former are the total spectra from which the acoustics is extracted, and the latter serves as reference. The spectrum obtained from filtering out the data measured at $U_\infty = 30 \text{ m s}^{-1}$ is very close to that directly measured without any flow. Leaving aside the troughs around 1400 and 1800 Hz, the two spectra are no more than 1 – 2 dB.Hz⁻¹ apart. On the other hand, increasing the velocity to 45 m s⁻¹ deteriorates the quality of the reconstructed spectrum; a possible explanation being the less favourable acoustic to

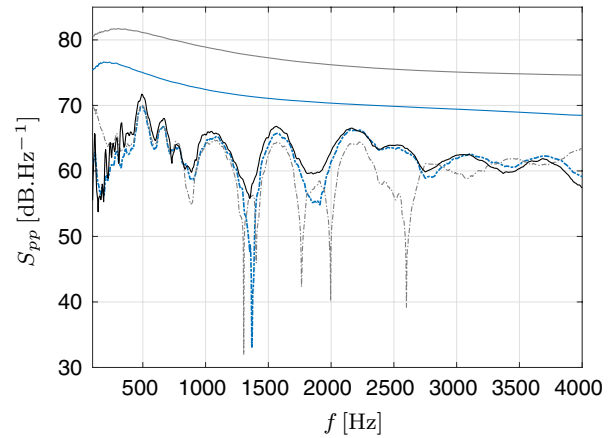


Fig. 13 S_{pp} on module 3 with acoustic source on: with flow at (—) 30 m s⁻¹, (—) 45 m s⁻¹ and (—) without flow; and acoustics filtered from $k_1 - \omega$ at (— · —) 30 m s⁻¹ and (— · —) 45 m s⁻¹

hydrodynamic energy ratio, on top of the distorted propagation through the flow.

6 Concluding remarks

Measurement of the wall pressure fluctuations has been conducted on a full-scale model of the fore part of a business jet. The antennas of MEMS microphones placed on three key locations provided repeatable and homogeneous data despite the complexity of the set-up. Frequency spectra were shown to strongly deviate from the classical Goody model, particularly for the two locations where the boundary layer was the thinnest.

Coherence was measured and the high spatial resolution enabled the study of its spatial decay. While an exponential decay is observed at any given frequency, the assumption of auto-similarity on one parameter $\omega r / U_c$ does not hold satisfactorily. This could be the explanation for the deviation from the -1 power law in the decay of coherence length scale with frequency. The present data indeed shows a steeper decay over a wide frequency range.

The spatial structure was also described in terms of wavenumber–frequency spectra that show well-defined convection ridges in good agreement with the convection velocity obtained from the phase of the cross-spectra. These spectra could be used in vibro-acoustics application as inputs to models for the load due to the pressure field.

Finally, the wavenumber–frequency formalism was used to perform spectral filtering and extract acoustic content

generated by a source from the wall pressure field. At moderate speed, an excellent match was found between the reconstructed spectrum and that measured with only acoustic waves and no flow.

Acknowledgements This project has received funding from the Clean Sky 2 Joint Undertaking under the European Union’s Horizon 2020 research and innovation programme under grant agreement no.717084. The authors would like to thank Floriane Rey from Dassault Aviation, and Romain Leneveu and Hugo Siwiak from Vibratec, for coordinating the overall project and overseeing the manufacturing of the mock-up. The authors are also grateful to Pascal Souchette for his support throughout the project. The authors are thankful for the fruitful discussion with the reviewers that led to expanding the appendix on sensors’ resonance. This work was performed within the framework of the Labex CeLyA of the Université de Lyon, within the programme ‘Investissements d’Avenir’ (ANR-10-LABX-0060/ANR-16-IDEX-0005) operated by the French National Research Agency (ANR).

Appendix A: Discussion of the Corcos correction

Using a sensor of finite size attenuates the measured spectrum, as formally shown by Corcos (1963). The attenuation can be written in an integral form where the integrand is the product of two contributions: the response of the transducer and the cross-spectrum of the pressure field. The former can be computed based on its size and shape, Corcos (1963) derived its expression for rectangular and circular sensors and Ko (1993) extended this work to other shapes using the wavenumber formalism. The latter can be modelled, which is the main motivation for the Corcos model, and the attenuation thus estimated. Figure 14 shows the attenuation computed with the transducer response given by Corcos for a circular sensor of diameter d_0 , and the cross-spectrum modelled by both the Corcos and Mellen models. The values tabulated by Corcos are also given.

No significant difference between the two used models can be seen below $\omega(d_0/2)/U_c = 2.5$. For high values of normalised frequency the attenuation is indeed strong, and although the models induce discrepancies in its estimation it remains of the same order. With the current set-up and taking $U_c = 0.6 \times U_e$ since it is difficult to measure at high frequencies, one obtains 0.51 and 1.52 for $\omega(d_0/2)/U_c$ at 5 and 15 kHz respectively. Despite the discussed limitations of the Corcos model in terms of the cross-spectral shape due to the separation of variable, it thus appears that it can satisfactorily be used for the correction of the attenuation due to the sensor size, and that the use of a more recent model does not provide significant changes.

Appendix B: Correction for the sensors’ resonance

Identification of the resonance

The INMP621 MEMS microphones exhibit a resonance at 20.5 kHz, before being installed on an electronic board. To check the nature of this resonance, two microphones have been placed on electronic boards of different thicknesses, one of 0.6 mm and one of 0.2 mm, with a pinhole larger than the sound port. Both sensors have been mounted on a flat plate in a wind tunnel, as illustrated in Fig. 15, and simultaneously recorded data at various inlet velocities. Figure 16 shows the spectra from both sensors at a given velocity. The resonance occurs at distinct frequencies, of which the ratio is 1.3.

Should this resonance be due to a cavity inside the MEMS sensors, one could make the following assumptions. First, let us suppose that a cavity of volume V is connected to the sound port of the sensor that acts as a neck in a Helmholtz configuration. Second, let us also consider that the added thickness of the PCBs only increases the length of the neck, without accounting for a change in diameter. The two configurations correspond to Helmholtz resonators with the same volume and necks of the same diameter but different lengths. The corresponding resonance frequencies follow:

$$f_{r,i} = \frac{c_0}{2\pi} \sqrt{\frac{\pi D^2/4}{V(L_{N,i} + \delta L_N)}} \quad \text{thus} \quad \frac{f_{r,1}}{f_{r,2}} = \sqrt{\frac{L_{N,2} + \delta L_N}{L_{N,1} + \delta L_N}}$$

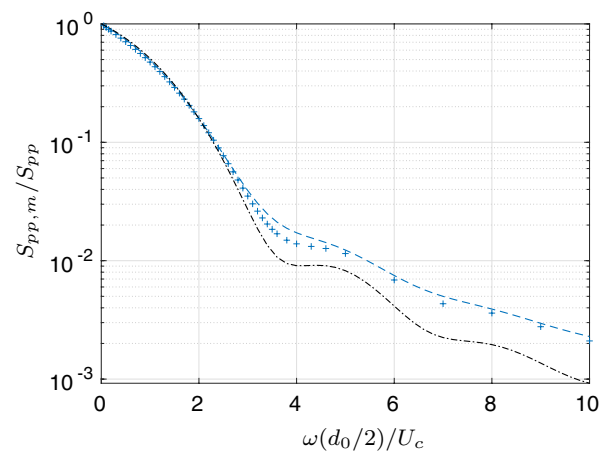


Fig. 14 Attenuation due to sensor size, using (— —) Corcos and (— · —) Mellen model, along with (+ +) the values tabulated by Corcos

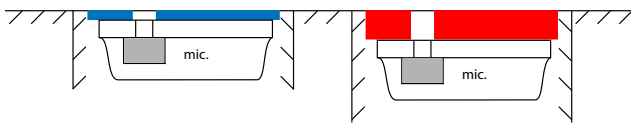


Fig. 15 Two identical sensors affixed on PCBs of different thicknesses and flush mounted onto a flat plate. The grey area corresponds to the front chamber. The sound port connects the front chamber to the PCB pinhole. PCB colors correspond to Fig. 16

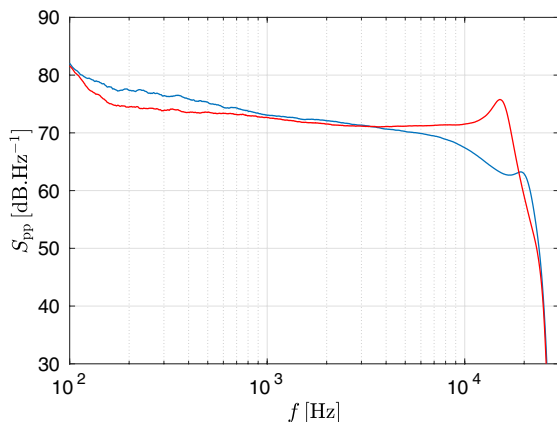


Fig. 16 Spectra for two MEMS installed on a thick (red) and thin (blue) PCB at 34 m s⁻¹

where c_0 is the speed of sound, D the diameter of the neck, L_N the length of the neck, V the cavity volume and δL_N the end correction of a flanged open pipe. Such correction is given for each open end by $0.41 \times D$ (Norris and Sheng 1989). In the present configuration, one has $\delta L_N = 0.82 \times D$, giving $f_1/f_2 = 1.3$. The observed resonance thus corresponds to the considered Helmholtz configuration.

There is indeed a small volume in the MEMS sensors, called the front chamber, between the membrane itself and the inner end of the sound port, as shown in Fig. 15. Taking $D = 0.25$ mm from the manufacturer specification, along with a 0.30 mm length of the sound port, and the resonance indicated at 20.5 kHz for a bare sensor, one obtains $V = 0.69$ mm³.

The authors have inspected a sample MEMS sensor, to obtain a section view. Although it is rather delicate to do so without damaging the parts, combining observations and technical documentation gives a rough estimate of the front chamber volume to about 1 mm³. While further measurements would be needed to know this exact volume, it is safe to say that this front chamber acts as the resonator volume in the discussed Helmholtz configuration.

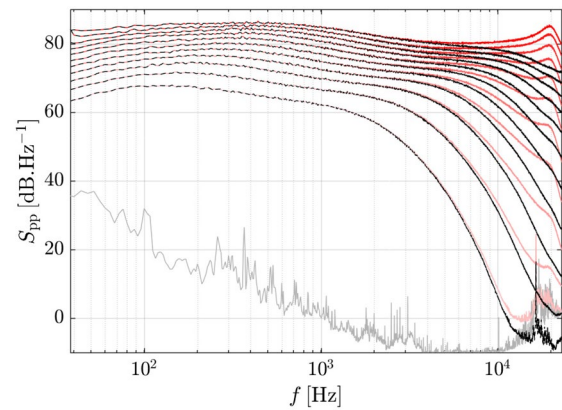


Fig. 17 Speed ramp-up of spectra for $U_\infty = 15 : 5 : 60$ m s⁻¹, with (black) and without (red) resonance correction, plus back ground noise

Correction of the spectra

Based on the previous discussion, the spectra (S_{pp}) measured in this study and presented in this paper have all been corrected using a second order resonator. The complex transfer function reads

$$H = \left[1 + i \frac{f}{qf_r} - \left(\frac{f}{f_r} \right)^2 \right]^{-1},$$

where q is a quality factor, f_r is the frequency of the resonance and $i^2 = -1$. The value $q = 4$ has been adjusted so that the spectra do not exhibit a non-physical change in their decay rate.

The effect of this correction is shown in Fig. 17 for inlet velocities (U_∞) ranging from 15 to 60 m s⁻¹. Although the effect is negligible for the lowest velocities, it is significant for the highest ones. In particular, for 45 m s⁻¹ spectra could not be discussed properly without this correction.

The background noise, that is the spectrum measured without flow nor acoustic source, is also given in Fig. 17. The difference with the spectra is close to 40 dB.Hz⁻¹ in the mid-frequency range, and only the spectra from 15 and 20 m s⁻¹ are altered, at high frequencies.

References

Arguillat B, Ricot D, Bailly C, Robert G (2010) Measured wavenumber: frequency spectrum associated with acoustic and aerodynamic wall pressure fluctuations. *J Acoust Soc Am* 128(4):1647–1655. <https://doi.org/10.1121/1.3478780>

Bhat W (1971) Use of correlation technique for estimating in-flight noise radiated by wing-mounted jet engines on a fuselage. *J Sound Vib* 17(3):349–355. [https://doi.org/10.1016/0022-460X\(71\)90647-X](https://doi.org/10.1016/0022-460X(71)90647-X)

- Bull MK (1996) Wall-pressure fluctuations beneath turbulent boundary layers: Some reflections on forty years of research. *J Sound Vib* 190(3):299–315. <https://doi.org/10.1006/jsvi.1996.0066>
- Catlett MR, Anderson JM, Forest JB, Stewart DO (2016) Empirical modeling of pressure spectra in adverse pressure gradient turbulent boundary layers. *AIAA J* 54(2):569–587. <https://doi.org/10.2514/1.J054375>
- Cohen E, Gloerfelt X (2018) Influence of pressure gradients on wall pressure beneath a turbulent boundary layer. *J Fluid Mech* 838:715–758. <https://doi.org/10.1017/jfm.2017.898>
- Corcos GM (1963) Resolution of pressure in turbulence. *J Acoust Soc Am* 35(2):192–199. <https://doi.org/10.1121/1.1918431>
- Eitel-Amor G, Örlü R, Schlatter P (2014) Simulation and validation of a spatially evolving turbulent boundary layer up to $Re_\theta = 8300$. *Int J Heat Fluid Flow* 47:57–69. <https://doi.org/10.1016/j.ijheafluidflow.2014.02.006>
- Esteban LB, Dogan E, Rodríguez-López E, Ganapathisubramani B (2017) Skin-friction measurements in a turbulent boundary layer under the influence of free-stream turbulence. *Exp Fluids* 58(9):115. <https://doi.org/10.1007/s00348-017-2397-8>
- Farabee TM, Casarella MJ (1991) Spectral features of wall pressure fluctuations beneath turbulent boundary layers. *Phy Fluids A Fluid Dyn* 3(10):2410–2420. <https://doi.org/10.1063/1.858179>
- Goody M (2004) Empirical spectral model of surface pressure fluctuations. *AIAA J* 42(9):1788–1794. <https://doi.org/10.2514/1.9433>
- Harun Z (2012) The structure of adverse and favourable pressure gradient turbulent boundary layers. Ph.D. thesis
- Haxter S, Spehr C (2012) Two-dimensional evaluation of turbulent boundary layer pressure fluctuations at cruise flight conditions. In: 18th AIAA/CEAS Aeroacoustics Conference, p. 2139. <https://doi.org/10.2514/6.2012-2139>
- Haxter S, Spehr C (2018) Up in the air: In-flight wavenumber characterization of surface pressure fluctuations at transonic conditions. In: 24th AIAA/CEAS Aeroacoustics Conference, p. 3275. <https://doi.org/10.2514/6.2018-3275>
- Hu N (2018) Empirical model of wall pressure spectra in adverse pressure gradients. *AIAA J* 56(9):3491–3506. <https://doi.org/10.2514/1.J056666>
- Hutchins N, Nickels TB, Marusic I, Chong M (2009) Hot-wire spatial resolution issues in wall-bounded turbulence. *J Fluid Mech* 635:103–136. <https://doi.org/10.1017/S0022112009007721>
- Ko SH (1993) Performance of various shapes of hydrophones in the reduction of turbulent flow noise. *J Acoust Soc Am* 93(3):1293–1299. <https://doi.org/10.1121/1.405414>
- KTH FLOW group: Turbulent boundary layers at various Re up to $Re_\theta = 8300$, les (2019). <https://kth.app.box.com/v/TBL-SIM-RE8000>
- Lee S (2018) Empirical wall-pressure spectral modeling for zero and adverse pressure gradient flows. *AIAA J* 56(5):1818–1829. <https://doi.org/10.2514/1.J056528>
- Maxit L (2016) Simulation of the pressure field beneath a turbulent boundary layer using realizations of uncorrelated wall plane waves. *J Acoust Soc Am* 140(2):1268–1285. <https://doi.org/10.1121/1.4960516>
- Mellen RH (1990) On modeling convective turbulence. *J Acoust Soc Am* 88(6):2891–2893. <https://doi.org/10.1121/1.399695>
- Norris A, Sheng I (1989) Acoustic radiation from a circular pipe with an infinite flange. *J Sound Vib* 135(1):85–93. [https://doi.org/10.1016/0022-460X\(89\)90756-6](https://doi.org/10.1016/0022-460X(89)90756-6)
- Prigent SL, Salze É, Bailly C (2019) Deconvolution of wave-number-frequency spectra of wall pressure fluctuations. *AIAA J* 58(1):1–10. <https://doi.org/10.2514/1.J058203>
- Rodríguez-López E, Bruce PJ, Buxton OR (2015) A robust post-processing method to determine skin friction in turbulent boundary layers from the velocity profile. *Exp Fluids* 56(4):68. <https://doi.org/10.1007/s00348-015-1935-5>
- Rozenberg Y, Robert G, Moreau S (2012) Wall-pressure spectral model including the adverse pressure gradient effects. *AIAA J* 50(10):2168–2179. <https://doi.org/10.2514/1.J051500>
- Salze É, Bailly C, Marsden O, Jondeau E, Juvé D (2014) An experimental characterisation of wall pressure wavevector-frequency spectra in the presence of pressure gradients. In: 20th AIAA/CEAS Aeroacoustics Conference, p 2909. <https://doi.org/10.2514/6.2014-2909>
- Salze E, Jondeau E, Pereira A, Prigent SL, Bailly C (2019) A new mems microphone array for the wavenumber analysis of wall-pressure fluctuations: application to the modal investigation of a ducted low-mach number stage. In: 25th AIAA/CEAS Aeroacoustics Conference, p 2574. <https://doi.org/10.2514/6.2019-2574>
- Schloemer HH (1967) Effects of pressure gradients on turbulent-boundary-layer wall-pressure fluctuations. *J Acoust Soc Am* 42(1):93–113. <https://doi.org/10.1121/1.1910581>
- Smol'yakov A (2006) A new model for the cross spectrum and wave-number-frequency spectrum of turbulent pressure fluctuations in a boundary layer. *Acoust Phys* 52(3):331–337. <https://doi.org/10.1134/S1063771006030146>
- Willmarth WW (1975) Pressure fluctuations beneath turbulent boundary layers. *Annu Rev Fluid Mech* 7(1):13–36. <https://doi.org/10.1146/annurev.fl.07.010175.000305>

Publisher's Note Springer Nature remains neutral with regard to jurisdictional claims in published maps and institutional affiliations.